Nanoscale

PAPER

View Article Online
View Journal | View Issue

Cite this: *Nanoscale*, 2025, **17**, 26417

A portable and versatile rGO-Co_3O_4-Pt nanocomposite-based electrochemical sensor for *ex vivo* and *in vivo* cardiac oxidative stress monitoring

Sima Singh,†[a] Stefania Melini,†[a] Ada Raucci,[a] Arshid Numan, *[b,c] Mohammad Khalid, [d,e] Bey Hing Goh,[f,g] Rosaria Meli,[a] Claudio Pirozzi*[a] and Stefano Cinti *[a,h,i]

The excessive production of reactive oxygen species (ROS) disrupts redox homeostasis, contributing to the development of cardiovascular diseases. Among ROS, hydrogen peroxide (H_2O_2) serves as a key mediator of oxidative signaling and a critical biomarker of cellular oxidative damage due to its relative stability and signaling relevance. However, current detection strategies for ROS and H_2O_2 often lack the necessary sensitivity, selectivity, and real-time responsiveness, underscoring the urgent need for advanced sensing platforms to support precision cardiovascular medicine. The research introduces a ROS detection based on reduced graphene oxide-cobalt oxide-platinum (rGO-Co_3O_4-Pt) nanocomposites for biological sample analysis. The nanocomposite platform enables H_2O_2 detection down to 160 nM, with linearity up to 2.50 μM. The platform showed acceptable analytical performance in terms of sensitivity, repeatability, and selectivity, which enabled both *ex vivo* and *in vivo* H_2O_2 monitoring. The method was validated in doxorubicin (DOX)-induced cardiotoxicity models using HL-1 cells and C57BL/6J mice, showing strong correlation with MTT-based ROS assays. The rGO-Co_3O_4-Pt nanocomposite improves portable analytical devices for real-world pharmacological applications. The technology enables real-time therapeutic monitoring while optimizing individualized dosing and expanding its applications to cancer treatment and diabetes management and neurological disorders.

Received 4th August 2025,
Accepted 2nd November 2025

DOI: 10.1039/d5nr03297k

rsc.li/nanoscale

1 Introduction

Chemically reactive molecules containing oxygen are known as reactive oxygen species (ROS).[1] These molecules are by-products of normal oxygen metabolism, including superoxide (O^{2-}), hydrogen peroxide (H_2O_2), hydroxyl radicals ($^{\bullet}OH$), and hypochlorite (ClO^-) and can function as signaling molecules due to their rapid responsiveness to various stimuli.[2] However, when their levels exceed the cell's defense mechanisms, ROS can induce harmful oxidative stress.[3] Oxidative stress damages cellular macromolecules such as lipids, proteins, and nucleic acids, leading to impaired cell function and eventual cell death.[4] This harmful process has been implicated in the pathogenesis of a wide array of diseases, including cancer, neurodegenerative disorders, and cardiovascular conditions.[5]

In the context of cardiovascular conditions, oxidative stress plays a pivotal role in the development of numerous conditions, such as atherosclerosis, myocardial infarction, and heart failure.[6] Excess of ROS not only directly damages cardiac cells but also triggers a cascade of inflammatory responses.[7] In cardiovascular disease, ROS can be generated by various

[a]*Department of Pharmacy, University of Naples Federico II, Via D. Montesano 49, 80131 Naples, Italy. E-mail: stefano.cinti@unina.it, claudio.pirozzi@unina.it*
[b]*Sunway Centre for Electrochemical Energy and Sustainable Technology (SCEEST), School of Engineering and Technology, Sunway University, No. 5 Jalan Universiti, Bandar Sunway, 47500 Petaling Jaya, Selangor Darul Ehsan, Malaysia. E-mail: numana@sunway.edu.my*
[c]*Department of Applied Physics, Saveetha School of Engineering, Saveetha University (SIMATS), Chennai, India*
[d]*Materials and Manufacturing Research Group, James Watt School of Engineering, University of Glasgow, Glasgow G12 8QQ, UK*
[e]*Centre for Research Impact and Outcome, Chitkara University, Punjab, India*
[f]*Sunway Biofunctional Molecules Discovery Centre (SBMDC), School of Medical and Life Sciences, Sunway University, Sunway City, Selangor, Malaysia*
[g]*Faculty of Health, Australian Research Centre in Complementary and Integrative Medicine, University of Technology Sydney, Ultimo, NSW, Australia*
[h]*Sbarro Institute for Cancer Research and Molecular Medicine, Center for Biotechnology, College of Science and Technology, Temple University, Philadelphia, PA 19122, USA*
[i]*Bioelectronics Task Force, University of Naples Federico II, Via Cinthia 21, 80126 Naples, Italy*
†These authors contributed equally to this work.

exogenous and endogenous factors such as environmental toxins, radiation, inflammation, and certain medications such as chemotherapeutic drugs.[8] Notably, the anthracycline doxorubicin (DOX) is a well-known inducer of oxidative stress, particularly in the heart.[9] Although, DOX is a highly effective antitumor agent used for treating various cancers, its clinical application is limited by its dose-dependent and cumulative cardiotoxicity, often referred to as the "Red Demon".[10] DOX triggers oxidative stress within cardiac cells by generating excessive ROS, which damages cellular components, leading to mitochondrial dysfunction and activation of apoptotic (programmed cell death) pathways. The resultant cell death contributes to the cardiac dysfunction, potentially culminating in acute heart failure.[11] Consequently, the mortality rate following DOX therapy ranges from 10 to 38% after a single or cumulative dose of 5–25 mg kg^{-1}, and increases significantly to 50% within two years after chemotherapy.[12] To mitigate DOX-induced cardiotoxicity, researchers are exploring strategies, including antioxidants,[13,14] nanotechnology,[15] gene therapies,[16,17] mitochondrial protection strategies,[18,19] and optimized chemotherapy regimens,[20] to reduce cardiac risk and enhance cardiac defenses. While these approaches are promising to reduce cardiotoxicity, the detection of ROS in DOX-induced cardiotoxicity stands out as a particularly effective strategy. Detecting elevated ROS levels serves as an early warning system for oxidative stress, enabling clinicians to intervene before significant cardiac damage occurs.[21] This proactive approach allows for timely treatment adjustments, such as modifying dosages or initiating protective therapies. Detecting ROS levels also helps in monitoring the effectiveness of interventions, risk stratification, and the development of targeted therapies.

In light of the strong link between DOX-induced cardiotoxicity and oxidative stress, measuring H_2O_2 levels in body fluids could serve as an indicator of oxidative stress in both physiological and pathological conditions.[22,23] However, clinical studies have yet to document H_2O_2 levels in DOX-induced cardiotoxicity. Efforts to measure H_2O_2 in tumor tissues are challenged by its low concentration, short half-life, and high chemical activity.[24] Regular monitoring of H_2O_2 levels would allow early detection of cardiac injury before irreversible damage occurs. Centralized laboratories techniques such as spectrophotometry,[25] chromatography,[26] Surface-enhanced Raman scattering (SERS),[27] chemiluminescence[28] and fluorimetry[29] have long been the gold standard for chemical and biomolecular analyses. However, the healthcare landscape is rapidly evolving due to social, economic, and technological transformations, with a focus on improving diagnostics accessibility, improving health standards, and ensuring timely interventions. Despite these advancements, many diagnostic technologies remain inaccessible in low-resource settings, prompting the World Health Organization (WHO) to establish the ASSURED criteria (affordability, sensitivity, specificity, user-friendliness, rapid and reliable performance, equipment-free operation, and deliverability) for global diagnostic platform development.[30] In response, recent technological innovations have witnessed a paradigm shift towards lab-on-chip (LOC) or point-of-care (POC) devices for various diagnostic applications. Among these, fluorometric and chemiluminescence techniques have been explored for detecting H_2O_2 levels *in ex vivo*. However, the low sensitivity of these techniques, along with the complexity of sample preparation, are a challenge for real-time, rapid measurements.[24]

Given these limitations, electrochemical biosensors offer a superior alternative, providing higher sensitivity, simpler sample preparation, and faster, real-time detection of H_2O_2.[31] Electrochemical biosensors are cost-effective and portable, aligning with WHO's ASSURED criteria for low-resource LOC or POC diagnostics. However, electrode performance can limit sensitivity and detection. Researchers are enhancing electrodes with nanomaterials, metal nanoparticles, and conductive polymers to improve catalytic efficiency and electron transfer, offering a viable alternative for improving detection sensitivity and selectivity. Modifying electrodes with appropriate materials has proven a viable alternative in boosting these characteristics.[32] In the literature, remarkable examples of nanomaterial-based electrochemical detection of H_2O_2 have been reported. For instance, Wang *et al.* detected H_2O_2 by modifying the electrode by AuNPs/ZIF-8@ZIF-67/GCE with high catalytic activity, with a wide detection range of 0.05–120 μM and low limit of detection (LOD) 0.016 μM.[33] In another study, Li and colleagues developed an electrochemical sensor using rROGO-S-Au HS/GCE for H_2O_2 detection, which demonstrated a wide range, low detection limit, and high sensitivity, making it promising for cancer diagnosis and real-time monitoring of tumor progression, with a LOD of 5 μM.[34] These studies highlight the capabilities of nanomaterials-based electrochemical sensor for detection of H_2O_2 reducing the fabrication complexity, lowering costs and enhancing scalability.

Among this, two-dimensional (2D) materials have emerged as a promising platform for developing flexible and ultrasensitive sensors. It is, therefore, not surprising that integrating functional nanomaterials with electrochemical devices enhances sensitivity and selectivity by tailoring surface functionalities for the detection of H_2O_2 in both *in ex vivo* and *in vivo* environments. Notably, graphene, often referred to as the "mother" of all 2D materials, stands out due to its biocompatibility and high electrical conductivity.[35] Despite its relatively recent development, reduced graphene oxide (rGO)/metal oxide nanocomposites have become the preferred choice for sensor development, offering enhanced surface area, improved conductivity, and greater stability.[36] rGO acts as an ideal support material due to its high conductivity, chemical stability, and ability to promote electron transfer. While rGO provides an excellent conductive matrix and large surface area, it lacks the catalytic activity, selectivity, and efficiency required for the sensitive H_2O_2 detection. The introduction of cobalt oxide (Co_3O_4) addresses the need for catalytic activity in redox reactions,[37] while platinum (Pt) enhances the reaction kinetics and sensitivity. Thus, we hypothesized that incorporating rGO, Co_3O_4, and Pt would significantly improve the sensitivity and selectivity of H_2O_2 detection. Here, we present

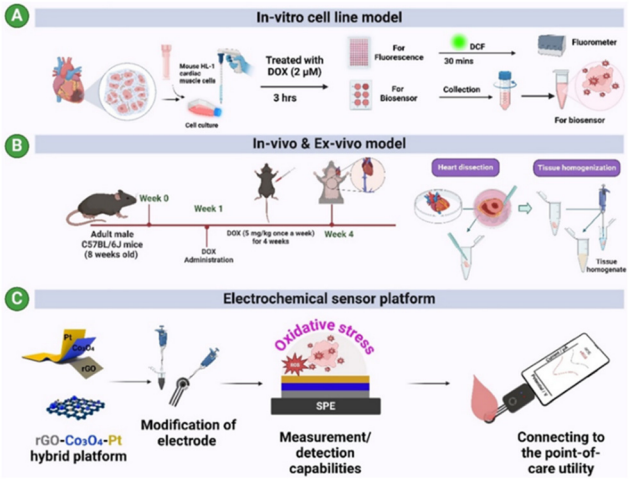

Scheme 1 Schematic representation of the experimental workflow. (A) Mouse HL-1 cardiac muscle cells are challenged with DOX as an *ex vivo* model of acute oxidative stress. (B) Adult male C57BL/6J mice are used for *in vivo* and *ex vivo* experiments to investigate chronic cardiotoxic effects of DOX, analyzing heart tissues for ROS determination. (C) An electrochemical sensor platform based on rGO-Co_3O_4-Pt is employed for sensitive detection of oxidative stress markers, enabling translation to point-of-care diagnostic applications.

a novel, decentralized and miniaturized printed electrochemical device modified with a rGO-Co_3O_4-Pt nanocomposite, for the real-time detection of ROS in both *ex vivo* and *in vivo* models, evaluating the oxidative stress induced by DOX treatment, which can lead to cardiotoxicity. The device demonstrates a remarkable accuracy in quantifying oxidative stress, advancing beyond current methods in managing and evaluating therapeutic efficacy, as illustrated in Scheme 1. The proposed multidisciplinary approach paves the way for new frontiers in pharmacological screening at the POC, reducing time-consuming and costly procedures. The case study described here represents the starting point for novel application, for both *in vivo* and implantable nanomodified analytical devices, for the pharmacological administration and the personalized therapies, aimed at improving therapy adherence and validating new treatments.

2 Experimental section

2.1 Chemicals and apparatus

Conductive inks (Ag/AgCl and graphite) were acquired from Acheson (Italy). Hydrogen peroxide, Acetaminophen, dopamine, glucose, ascorbic acid, and *tert*-butyl hydroperoxide, sodium acetate, potassium chloride, and potassium ferrocyanide were procured from Sigma Aldrich (Italy). Cobalt acetate tetrahydrate, platinum chloride, ammonia water, and ethanol were procured from Sigma Aldrich (Malaysia). All the chemicals used in this study were of analytical grade and used without additional processing or modification. Electrochemical analysis was executed employing a PalmSens portable potentiostat (Palm Instruments, The Netherlands). The complete electrochemical experiments were accomplished at room temperature. All the working solutions were prepared with double-distilled water from Millipore.

2.2 *Ex vivo* cell culture and reagents

Mouse HL-1 cardiac muscle cells (Merck Millipore) were cultured in 75 cm^2 culture flasks (Falcon, Germany) that had been precoated with a solution of 0.02% gelatin (Sigma Chemical, cat. number: G-9391) and 5 μg mL^{-1} fibronectin (Sigma Chemical, cat. number: F-1141) to promote cell adhesion and ensure optimal growth conditions. The cells were maintained in Claycomb medium (cat. number 51800C, Sigma Aldrich), specifically formulated for HL-1 cell growth. This medium was supplemented with 2 mM glutamine (L-glutamine, cat. number: A29168-01, Gibco), 100 U mL^{-1} penicillin, and 100 μg ml^{-1} streptomycin (PenStrep, cat. number: 15140-122, Gibco) to maintain sterility and prevent bacterial contamination. Additionally, 100 μM norepinephrine (Sigma Chemical) was added to support cellular function, and 10% Fetal Bovine Serum (FBS, cat. number: 16000044, Gibco) was included to provide necessary growth factors and nutrients. For cardiotoxicity experiments, DOX was sourced from Sigma-Aldrich, Segrate, Milan, Italy. It was dissolved in dimethyl sulfoxide (DMSO, Sigma-Aldrich, Segrate, Milan, Italy) to prepare a solution suitable for experimental use. DOX was employed as a model compound to study the cardiotoxic effects of chemotherapy drugs on cardiac cells.

2.3 Manufacturing of polyester-based printed strips

Screen-Printed Electrodes (SPEs) were manufactured on a polyester substrate using a semi-automatic screen-printing system (Model GPE/2; Type AP05). The fabrication involved two main steps, conducted at 100 °C for 30 minutes. First, a pseudo-reference electrode was printed using silver ink (Ag/AgCl, Electrodag 477 SS) and dried in an oven at 100 °C for 30 minutes. Next, the working and counter electrodes were printed with graphite ink (Elettrodag 421) under controlled environmental conditions. The working electrode featured a diameter of 0.4 cm, resulting in a geometric area of 0.07 cm^2. Prior to electrochemical experiments, adhesive tape was applied to define the contact area of the electrode and to insulate the electrical connections.

Synthesis of rGO-Co_3O_4. Graphene oxide (GO) was prepared following a simplified version of Hummers' method, as described in the previous work.[38] For the synthesis of reduced graphene oxide-cobalt oxide (rGO-Co_3O_4), 1 mmol of cobalt acetate tetrahydrate was dissolved in 10 mL of deionized (DI) water and then gradually added to a 20 mL suspension of GO (1 mg mL^{-1}) under constant stirring. Subsequently, 5 mL of a platinum chloride solution was introduced into the mixture while stirring continuously. After stirring for 30 minutes, 15 mL of ammonia solution was added dropwise with continuous stirring. The mixture was then stirred for an additional 30 minutes and transferred to a 100 mL Teflon-lined autoclave for a microwave-assisted hydrothermal reaction at 180 °C for 10 minutes, with a heating rate of 5 °C per minute. The result-

ing precipitate was collected, thoroughly washed with DI water and ethanol, and freeze-dried. The same procedure was applied for synthesizing rGO-Co_3O_4 and Co_3O_4, both with and without the addition of platinum salt and GO, respectively.

2.4 Characterization

The morphological characteristics of the individual specimens —Co_3O_4, rGO-Co_3O_4, and the rGO-Co_3O_4-Pt nanocomposite- were analyzed using a Hitachi TEM system integrated with an energy-dispersive X-ray spectrometer (EDX/EDS). X-ray diffraction (XRD) measurements were conducted on a PANalytical X'Pert3 powder diffractometer, utilizing Cu-Kα radiation (λ = 0.15406 nm) at 40 kV and 30 mA, covering a 2θ range of 5–80°. The surface properties of the rGO-Co_3O_4-Pt nanocomposite were characterized using a Thermo Scientific K-Alpha XPS system, maintained at a chamber pressure below 5×10^{-9} mbar. The instrument operated in large-area XL magnetic lens mode with pass energies set at 150 eV for survey scans and 20 eV for high-resolution scans. Spectra were acquired at a 90° electron take-off angle relative to the surface plane, with high-resolution peaks fitted using the algorithms provided in the ThermoVG Avantage software. Binding energies were determined by referencing the internal C1s signal at 284.9 eV.

2.5 Preparation of rGO-Co_3O_4-Pt nanocomposite dispersion

DI was used to prepare rGO-Co_3O_4-Pt nanocomposite aliquots at a concentration of 1 mg mL^{-1}. These aliquots were subsequently employed to modify the working electrode for further electrochemical studies. A 8 μL from each aliquot was applied onto the taped SPEs to fabricate the electrode.

2.6 Electrochemical measurements

The PalmSens4 portable potentiostat/galvanostat/impedance analyzer was used for conducting electrochemical measurements using a 100 μL drop of the working solution. First the cyclic voltammetry (CV) and electrochemical impedance spectroscopy (EIS) experiments were conducted to evaluate the electrochemical performance of the bare SPEs, rGO/SPEs, Co_3O_4/SPEs, Pt/SPEs, rGO-Co_3O_4/SPEs, and rGO-Co_3O_4-Pt/SPEs. The electrolyte used for these tests was a 5 mM solution of potassium ferricyanide/potassium ferrocyanide $[Fe(CN)_6]^{3-/4-}$ in 0.1 M KCl. Additionally, square wave voltammetry (SWV) experiments were performed with rGO-Co_3O_4-Pt/SPEs in 0.1 M KCl containing up to 2.5 μM hydrogen peroxide.

The same electrochemical technique was employed to measure ROS levels in HL-1 cardiomyocytes (control and DOX-treated cells) as well as in heart tissue obtained from mice treated with DOX (20 mg kg^{-1}) or control. In both *ex vivo* cell-line studies and *in vivo* animal experiments, 80 μL of cells or tissue resuspended in Dulbecco's PBS solution was applied to the working area of the rGO-Co_3O_4-Pt/SPEs.

2.7 Cell viability assay

The methyl-thiazolyl-tetrazolium (MTT) reagent was used to assess cell viability by detecting functional mitochondria in living cells. HL-1 cells (1.5×10^4 cells per well) were seeded into 96-well plates, starved in serum-free medium for 6 hours, and subsequently incubated with 2–5 μM DOX for 4 hours. Control cells were treated with 0.1% DMSO. Next, 5 μL of MTT reagent (5 mg mL^{-1}) was added to each well, followed by incubation at 37 °C for 4 hours. Formazan salts produced were dissolved by adding 100 μL of a solution containing 50% (v/v) *N*,*N*-dimethylformamide and 20% (w/v) sodium dodecyl sulfate (pH 4.5). After 24 hours of incubation at 37 °C, absorbance was measured at 550 nm. Viability variations were determined by normalizing the optical density (OD) values of treated cells to those of the controls.

2.8 Measuring cellular ROS *via* fluorescence

Cellular ROS levels were assessed using fluorescence in cells plated in 96-well microtiter plates at a density of approximately 2×10^4 cells per well. After a 6-hour incubation, the cells were stimulated by exposing them to 2 μM DOX for 3 hours, inducing oxidative stress and inflammatory damage. ROS production triggered by DOX was evaluated through intracellular detection of the fluorescent probe 2′,7′-dichlorofluorescein (DCF). Inside the cells, DCF undergoes hydrolysis by esterases, which remove its acetate group, trapping the probe within the cytoplasm. Oxidation of DCF produces fluorescence directly proportional to the total ROS generated. In this assay, HL-1 cells exposed to DOX were incubated with 5 μM DCF in DMSO for 30 minutes at 37 °C in the dark. Afterward, the cells were rinsed twice with 1× PBS, and fluorescence was measured using the Promega GloMax Explorer Microplate Reader with excitation and emission wavelengths of 488 nm and 525 nm, respectively. ROS levels were quantified using a DCF standard curve prepared in DMSO (0–1 mM).

For electrochemical ROS analysis, cells were seeded in P6-well plates at a density of 5.0×10^5 cells per well. After reaching 70–80% confluence, the cells were serum-starved in a serum-free medium for 6 hours before being stimulated with DOX under the same conditions described above. Following 3 hours of DOX treatment, the cells were collected in 1× PBS, and ROS levels were measured using electrochemical biosensors.

2.9 *In vivo* animal study

Eight-week-old adult male C57BL/6J mice were procured from Charles River Laboratories in Milan, Italy. The mice were assigned to experimental groups and received DOX at a dosage of 5 mg kg^{-1} *via* intraperitoneal (i.p.) injection once a week for 4 weeks, resulting in a total cumulative dose of 20 mg per kg per animal. At the end of the study, the mice were humanely euthanized under general anesthesia with 2.5% isoflurane inhalation, followed by cervical dislocation. Heart tissues were collected and homogenized in PBS 1× (40 mg of tissue per 100 μl) to measure ROS levels using biosensors.

All animal care and experimental procedures were conducted in accordance with both national and international guidelines and approved by the Local Animal Care Office (Centro Servizi Veterinari, University of Naples Federico II, Italy) and the Italian Ministry of Health under protocol no. 36/2024-PR on January 9, 2024. Animal studies were performed

in compliance with the Italian D.L. (No. 26 of 4 March 2014) of the Italian Ministry of Health and the EU Directive 2010/63/EU for animal experiments, ARRIVE guidelines 2.0, and the Basel declaration, including the 3Rs concept.

2.10 Statistical analysis

Data are reported as mean ± SEM. Normality was assessed using the Shapiro–Wilk test. For both *ex vivo* and *in vivo* experiments, comparisons between two groups were evaluated with an unpaired Student's *t*-test. *In vivo* analyses used n = 5–6 animals per group; in *ex vivo* results derive from three independent experiments, each performed in duplicate. Statistical significance was set at $p < 0.05$. All analyses were performed in GraphPad Prism 10 (GraphPad Software, San Diego, CA, USA).

3 Results and discussion

3.1 Morphological characterization

Morphological characterization was conducted using high-resolution transmission electron microscopy (HRTEM), selected area electron diffraction (SAED), and energy-dispersive X-ray spectroscopy (EDS). HRTEM analysis provided detailed insights into the physical structure of the nanomaterials across various fabrication stages. Fig. 1A, with a magnified inset, shows the well-defined cubic morphology of Co_3O_4. This nanocubic structure is recognized for its superior electrochemical performance, enhancing electron transport and providing multiple active sites during catalytic reactions.[39] Fig. 1B presents the rGO-Co_3O_4 nanocomposite, where the cubic morphology of Co_3O_4 is retained but dispersed across the rGO sheet. The rGO acts as a conductive substrate with a high surface area, facilitating uniform nanoparticle distribution and preventing aggregation.[40] Fig. 1C depicts the rGO-Co_3O_4 nanocomposite modified with Pt nanoparticles (rGO-Co_3O_4-Pt), revealing cubic Co_3O_4 nanoparticles decorated with smaller Pt nanoparticles. It is evident from Fig. 1D, that the Pt nanoparticles were decorated on the cubical surface of Co_3O_4. The incorporation of Pt enhances catalytic properties by improving the availability of reactive sites on the rGO-Co_3O_4 surface.[41] The selected area electron diffraction (SAED) pattern (Fig. 1D inset) reveals the crystallinity and phase structure of the rGO-Co_3O_4-Pt nanocomposite. Energy-dispersive X-ray spectroscopy (EDX) analysis (Fig. 1E) identifies the elemental composition of the rGO-Co_3O_4-Pt sample. The spectrum shows peaks for carbon (C) from rGO, oxygen (O) from rGO and Co_3O_4, cobalt (Co) from Co_3O_4, and platinum (Pt) from nanoparticles, confirming the formation of the rGO-Co_3O_4-Pt nanocomposite. Elemental maps depict the distribution of these elements in the material.

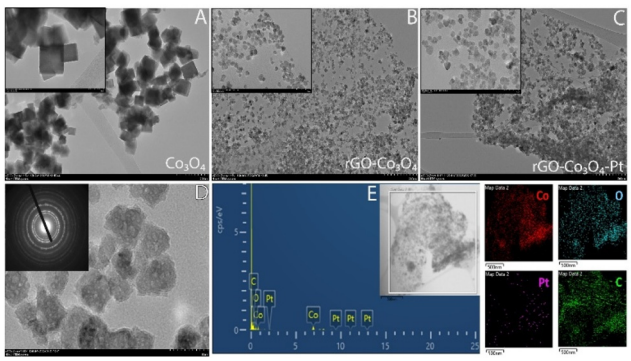

Fig. 1 Characterization of the rGO-Co_3O_4-Pt nanocomposites. (A) TEM image of Co_3O_4 nanoparticles displaying cubic morphology. (B) TEM image of the rGO-Co_3O_4 nanocomposites, indicating uniform distribution of Co_3O_4 nanoparticles on graphene sheets. (C) TEM image of the rGO-Co_3O_4-Pt nanocomposites, demonstrating the integration of Pt nanoparticles. (D) High-resolution TEM and SAED patterns confirm the crystalline structure of Co_3O_4 and Pt. (E) EDS analysis verifies the presence of Co, Pt, O, and C, with elemental mapping illustrating their spatial distribution within the nanocomposites.

3.2 Structural characterizations

The X-ray diffraction (XRD) patterns of the three samples-Co_3O_4 (red), rGO-Co_3O_4 (black), and rGO-Co_3O_4-Pt (blue)-exhibit characteristic diffraction peaks corresponding to the distinct phases of the materials, as shown in Fig. 2A.

The primary diffraction peaks of Co_3O_4 are observed at 2θ values of approximately 19° (111), 31.5° (220), 36.8° (311), 45° (400), 59.3° (422), and 65.2° (511), indicating a high degree of crystallinity. These results are consistent with the reported in the literature.[42,43] The XRD pattern of the rGO-Co_3O_4 sample exhibits peaks characteristic of Co_3O_4 with slightly reduced intensity compared to pure Co_3O_4. This reduction aligns with prior findings on the impact of rGO on the crystallization behavior and structural properties of nanocomposites. The XRD pattern of the rGO-Co_3O_4-Pt sample shows minor changes in peak intensities. However, distinct Pt diffraction peaks are not observed, likely due to overlap with Co_3O_4 peaks or the low Pt content producing weak signals.

The rGO-Co_3O_4-Pt nanocomposite surface was analyzed using X-Ray Photoelectron Spectroscopy (XPS) to determine

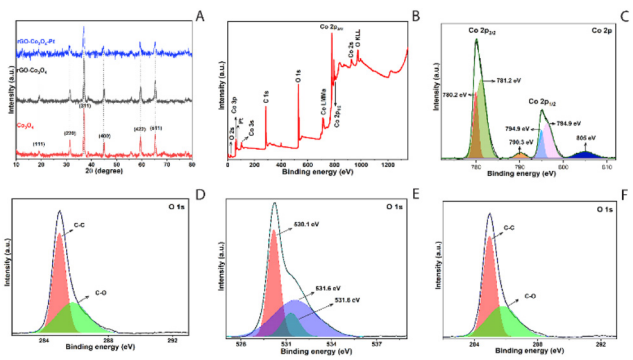

Fig. 2 Characterization of rGO-Co_3O_4-Pt nanocomposites by XRD and XPS. (A) XRD patterns confirm the crystalline structure of Co_3O_4 and the incorporation of rGO and Pt nanoparticles into the nanocomposites. (B and C) XPS spectra of Co $2p_{3/2}$ indicate and Co 2p. (D–F) XPS O 1s spectra.

the structure and valence states of carbon (C), oxygen (O), cobalt (Co), and platinum (Pt), as shown in Fig. 2(B–F). The prominent C 1s peak at 284.5 eV confirms the presence of sp^2-hybridized carbon in the rGO framework, indicating the effective reduction of GO.[44] The O 1s peak at 530–532 eV corresponds to oxygen, originating from the Co_3O_4 phase and residual oxygen-containing functional groups in the rGO structure.[42,45] The Co $2p_{3/2}$ and Co $2p_{1/2}$ peaks at approximately 780 and 795 eV are characteristic of cobalt in Co_3O_4, reflecting a combination of Co^{2+} and Co^{3+} oxidation states.[46] The observed peaks confirm the formation of cobalt oxide in the nanocomposite. A weak peak at 70–80 eV verifies the presence of platinum in the sample.[47,48] The analysis shows that Co_3O_4 and Pt effectively functionalized the rGO matrix, forming a well-integrated rGO-Co_3O_4-Pt nanocomposite.

3.3 Electrochemical characterization of the rGO-Co_3O_4-Pt nanocomposite as a sensing platform

CV and EIS studies were performed to evaluate the electrochemical behavior of bare SPE and modified electrodes (rGO/SPE, Co_3O_4/SPE, Pt/SPE, rGO-Co_3O_4/SPE, and rGO-Co_3O_4-Pt/SPE) in 5 mM $[Fe(CN)_6]^{3-/4-}$ solution prepared in 0.1 M KCl. The electrochemical behavior of the electrodes was evaluated using CV by comparing the cathodic peak current (I_{pc}) and the potential difference (ΔE) between the anodic and cathodic peaks, as shown in Fig. 3A.

The unmodified SPE exhibited the lowest cathodic current (I_{pc} = −34 μA; ΔE = −0.4 V), indicating slow electron transfer kinetics and low electrochemical activity. Modifying the electrode with nanocomposites improved performance. rGO/SPE showed a slight improvement (I_{pc} = −41 μA, ΔE = −0.3 V), while Co_3O_4/SPE demonstrated further enhancement (I_{pc} = −48 μA, ΔE = −0.2 V). Pt/SPE achieved I_{pc} = −53 μA with ΔE = −0.2 V. The rGO-Co_3O_4/SPE modification resulted in the highest current (I_{pc} = −64 μA) and a low ΔE of −0.2 V. The rGO-Co_3O_4-Pt/SPE electrode exhibited the highest performance, with I_{pc} = −87 μA and ΔE = −0.3 V, reflecting significant improvements in electron transfer kinetics and reaction reversibility compared to the bare SPE and other modifications. The CV curves show well-defined oxidation and reduction peaks for the redox species, confirming that the electrode operates *via* a surface-controlled process.

The Nyquist plot of EIS (Fig. 3B) reveals charge transfer resistance (R_{ct}) and electrochemical behavior. The bare SPE (black) showed the largest semicircle, indicating the highest R_{ct} and poor conductivity. Modified electrodes exhibit progressively smaller semicircles, reflecting improved performance. The rGO/SPE (red) shows reduced R_{ct}, while Co_3O_4/SPE (blue) and Pt/SPE (green) further decrease impedance. The rGO-Co_3O_4/SPE (orange) demonstrates significant improvement due to synergistic effects, and rGO-Co_3O_4-Pt/SPE (olive green) has the smallest semicircle, indicating the lowest R_{ct}.

The CV and EIS data demonstrate that the rGO-Co_3O_4-Pt nanocomposite exhibits enhanced current response and reduced charge transfer resistance, making it highly suitable for electrochemical sensing applications.

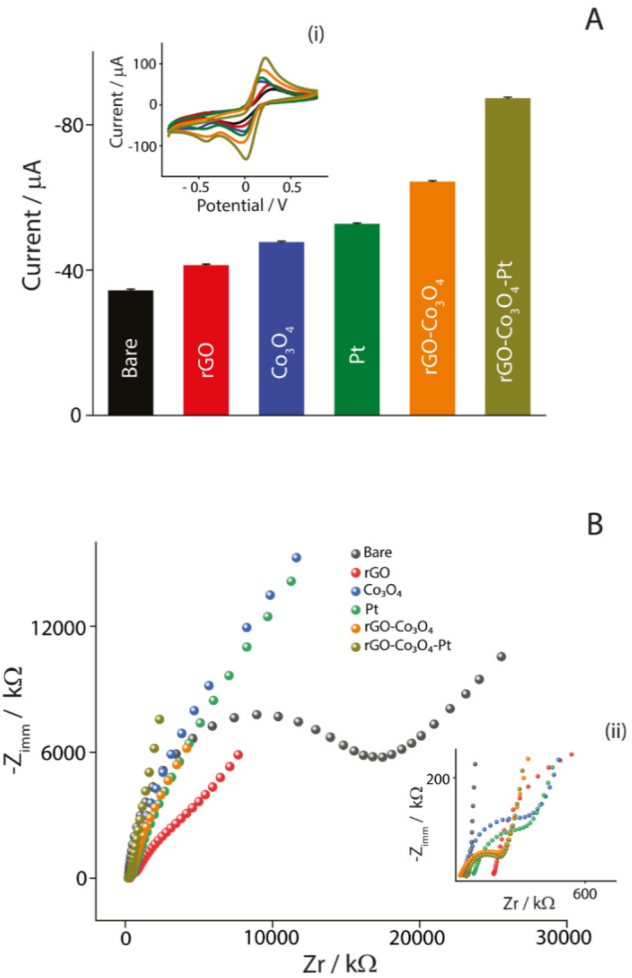

Fig. 3 Electrochemical performance evaluation of various electrode configurations: bare SPE (black), rGO/SPE (red), Co_3O_4/SPE (blue), Pt/SPE (green), rGO-Co_3O_4/SPE (orange), and rGO-Co_3O_4-Pt/SPE (olive green). (A) CV results presented as a bar graph showing peak current responses for each electrode. Insert (i) CV curves of the individual electrodes. Experimental conditions for CV: $t_{equilibration}$ = 0 s, E_{begin} = −0.8 V, $E_{vertex1}$ = −0.8 V, $E_{vertex2}$ = 0.8 V, E_{step} = 0.01 V, scan rate = 0.05 V s^{-1}. (B) Nyquist plots of EIS data. Insert (ii) magnified view of the low-resistance region. Experimental conditions: frequency range from 0.1 Hz to 65 000 Hz with 59 points. Both EIS and CV were conducted in 0.1 M KCl containing 5 mM $[Fe(CN)_6]^{3-/4-}$.

3.4 Electrochemical behavior toward H_2O_2 detection

Cyclic voltammograms were recorded in 0.1 M KCl with and without 5 mM H_2O_2 (Fig. 4A–F). The bare SPE showed only a slight increase in cathodic current (−16 ± 0.2 to −21 ± 0.4 μA), indicating poor catalytic activity. Introducing rGO gave a modest improvement (−11 ± 0.4 to −22 ± 0.3 μA), whereas Co_3O_4 produced a more substantial change, nearly doubling the current (−18 ± 0.4 to −35 ± 0.4 μA), consistent with its intrinsic electrocatalytic role. Pt modification enhanced the response further (−22 ± 0.2 to −51 ± 0.4 μA), as expected for peroxide reduction. The rGO-Co_3O_4 composite increased the signal again (−23 ± 0.2 to −54 ± 0.2 μA), reflecting complementary conductivity and cobalt redox activity. The ternary

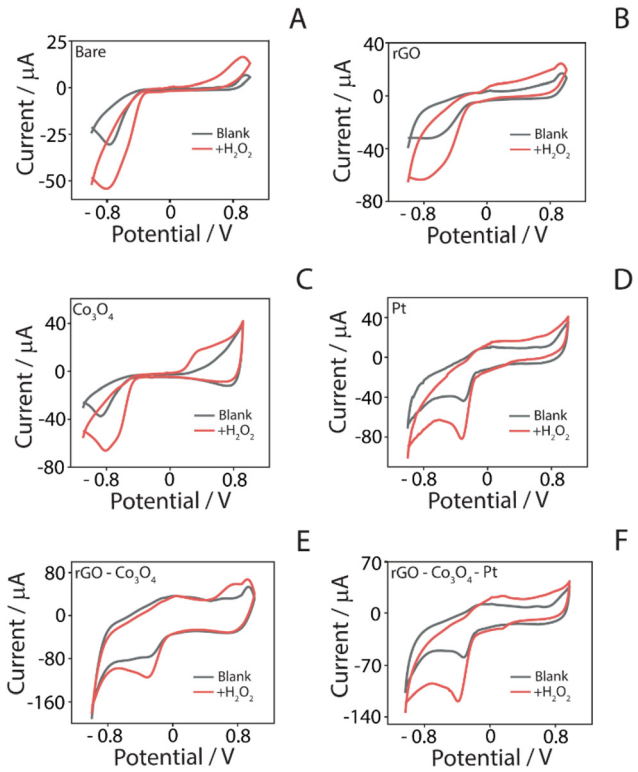

Fig. 4 Comparative CV response of different electrodes (A) bare and modified with (B) rGO, (C) Co_3O_4, (D) Pt, (E) rGO-Co_3O_4 and (F) rGO-Co_3O_4-Pt in 0.1 M KCl solution with or without adding 5 mM H_2O_2. Experimental conditions: $t_{equilibration}$ = 0 s, E_{begin} = −0.8 V; $E_{vertex1}$ = −0.8 V; $E_{vertex2}$ = 0.8 V; E_{step} = 0.01 V; scan rate = 0.05 V s^{-1}.

rGO-Co_3O_4-Pt nanocomposite delivered the largest response (−31 ± 0.3 to −71 ± 0.4 µA), underscoring the combined benefits of high conductivity, accessible redox sites, and catalytic efficiency. Together, these trends clarify the contribution of each component and highlight the superior performance of the integrated ternary system.

3.5 Sensing principle

The SPE modified with rGO-Co_3O_4-Pt nanocomposites exhibits the highest redox activity compared to the bare electrode and electrodes modified with rGO, Co_3O_4, Pt, or rGO-Co_3O_4 composites. The CV results revealed that the bare SPE exhibited minimal redox activity, indicating its limited ability to catalyze the electrochemical reduction of H_2O_2. However, modification with rGO nanomaterial significantly enhanced catalytic activity due to its two-dimensional structure.[49] Similarly, Co_3O_4/SPE demonstrated improved charge transfer properties by providing Co^{2+}/Co^{3+} sites that enhance electron transfer reactions, thereby boosting catalytic activity for H_2O_2 reduction.[50] Platinum nanoparticles provide highly active sites for the direct, low-overpotential, two-electron electroreduction of H_2O_2, giving early onset and large cathodic currents in neutral/alkaline media. The appropriate half-reaction for near-neutral conditions is:[51]

$$H_2O_2 + 2^{e-} \rightarrow 2OH^-$$

H_2O_2 can be reduced on Co_3O_4 *via* an inner-sphere CE/ECE pathway that keeps cobalt out of the net stoichiometry. H_2O_2 adsorbs at basic lattice-oxygen sites (enhanced by O-vacancies), deprotonates to a surface hydroperoxo (≡Co–OOH), then undergoes coupled electron-transfer steps to complete the two-electron reduction.[52,53] Together, electrically wired parallel pathways on Pt and Co_3O_4, enabled by the rGO scaffold, yield superior sensitivity, faster electron transfer kinetics, and a lower operating potential for the rGO-Co_3O_4-Pt nanocomposite compared with bare, rGO only, Co_3O_4 only, Pt only, or rGO-Co_3O_4 electrodes.

3.6 Analytical performance in standard solutions

Concentration studies up to 5 mM were conducted using the CV technique at a scan rate of 50 mV s^{-1} (Fig. 5A), following the confirmation of the strong electrocatalytic performance of rGO-Co_3O_4-Pt/SPEs for H_2O_2 reduction. The CV curves reveal a linear rise in peak current with increasing H_2O_2 concentrations (see insert i), signifying a diffusion-controlled electrochemical process. This indicates the effective interaction of H_2O_2 with the electrode surface, enabled by the high surface area of rGO, the catalytic properties of Co_3O_4, and the enhanced sensitivity provided by Pt. A sensitivity of 6.01 ± 0.17 µA mM^{-1} (R^2 = 1) indicated a strong linear correlation between cathodic current and hydrogen peroxide concentration. However, CV is less suitable for quantitative analysis due to lower sensitivity, broader peaks, and higher background currents, which reduce the accuracy. To overcome these limitations, SWV was used, offering sharper peaks, enhanced faradaic signals, and reduced background interference for improved quantitative analysis.[54]

The rGO-Co_3O_4-Pt/SPEs exhibit a sharp increase in peak current with increasing H_2O_2 concentrations (up to 2.5 µM) in 0.1 M KCl, as shown in Fig. 5B. The linear calibration curve in the inset (insert ii) confirms the sensitivity of the modified

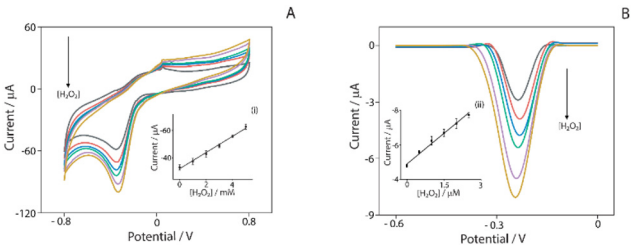

Fig. 5 Electrochemical response of rGo-Co_3O_4-Pt/SPEs for H_2O_2 detection at different concentrations: (A) CV studies of rGo-Co_3O_4-Pt/SPEs using concentrations of hydrogen peroxide up to 5 mM. Inset (i) illustrates the linear relationship between the current and H_2O_2 concentration. Experimental conditions: $t_{equilibration}$ = 0 s, E_{begin} = −0.8 V; $E_{vertex1}$ = −0.8 V; $E_{vertex2}$ = 0.8 V; E_{step} = 0.01 V; scan rate = 0.05 V s^{-1}. (B) SWV of the electrochemically activated rGo-Co_3O_4-Pt/SPEs in 0.1 M KCl containing different concentrations of H_2O_2 (up to 2.5 µM). Insert (ii) shows the calibration curve of current *versus* H_2O_2 concentration, confirming a strong linear correlation in the lower micromolar range. Experimental conditions: $t_{equilibration}$ = 0 s, E_{begin} = 0.0 V; E_{end} = −0.6 V, E_{step} = 0.001 V; with an amplitude of 0.025 V and a frequency of 25.0 Hz.

electrode for H_2O_2 detection, demonstrating a direct correlation between peak current and H_2O_2 concentration. This linearity suggests diffusion-controlled electrochemical behavior, consistent with other rGO-based composites, where high surface area and conductivity enhance electron transfer. The increased sensitivity shows that SWV is better than CV for precise analysis. The LOD was calculated using the formula LOD = $3\sigma_B/s$, where σ_B represents the standard deviation calculated for blank measurements, and s is the slope of the calibration curve. The limit of quantification (LOQ) was calculated as LOQ = 3.3 × LOD. In this study, the blank measurement standard deviation was 0.06, giving an LOD of about 160 nM and an LOQ of 0.54 μM. The performance of the rGO-Co_3O_4-Pt composite in detecting H_2O_2 was compared to several other reported H_2O_2 sensors (Table 1).

As summarized in Table 1, the rGO–Co_3O_4–Pt/SPE platform complements state-of-the-art H_2O_2 sensors not only in analytical sensitivity but, critically, in stability, selectivity, and *in vivo* usability. Selectivity is maintained at the low operating potential used here, with minimal response to common electroactive interferents in complex matrices, contrasting with many reports optimized primarily in simple electrolytes. Most notably, our sensor supports continuous measurements in biologically relevant settings (cardiomyocytes and murine heart-tissue homogenate, with *in vivo* validation), whereas a substantial fraction of Table 1 examples is limited to buffer, environmental, or benchtop biological models without *in vivo* operation.

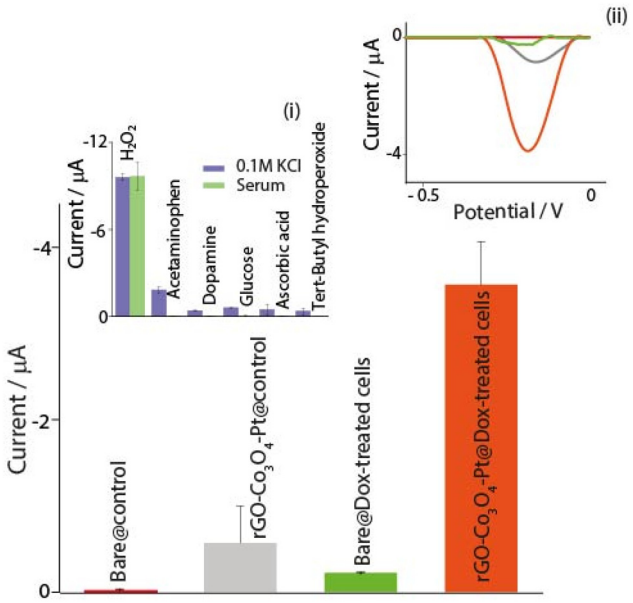

Fig. 6 The electrochemical detection of ROS in DOX-treated and control HL-1 cardiomyocyte cells. Inset (i) the bar graph shows the selectivity of rGO-Co_3O_4-Pt nanocomposite sensor for H_2O_2 compared to others Acetaminophen, dopamine, glucose, ascorbic acid, and *tert*-butyl hydroperoxide in 0.1 M KCl solution and serum; inset (ii) SWV curves for DOX-treated and control HL-1 cardiomyocyte cells. Experimental conditions: $t_{equilibration}$ = 0 s, E_{begin} = 0.0 V; E_{end} = −0.6 V, E_{step} = 0.001 V; with an amplitude of 0.025 V and a frequency of 25.0 Hz.

3.7 Selectivity study

Selectivity of the printed rGO-Co_3O_4-Pt/SPEs strips was assessed against common electroactive interferents (5 μM each; Fig. 6, insert i) in both 0.1 M KCl and serum. Hydrogen peroxide elicited a pronounced cathodic response (≈−10 μA), whereas Acetaminophen, dopamine, glucose, ascorbic acid, and *tert*-butyl hydroperoxide produced signals near baseline. The small currents observed for the other interferents were each less than 10% of the H_2O_2 response, confirming the high selectivity of the sensor toward H_2O_2. The close agreement between buffer and serum measurements indicates minimal matrix effects, supporting applicability of the sensor in biological environments.

Table 1 Electrochemical sensors for H_2O_2 detection

Electrode material	Technique	Detection limit (μM)	Linearity range (μM)	Real-sample application	Ref.
Graphene with MOF-on-MOF nanozymes	CV and EIS	0.06	0.1–3800	Human gingival crevicular fluid samples; environmental water	55
Fe_3O_4/graphene on carbon cloth	CV and EIS	4.79	10–110	Not specified	56
Pt nanoparticles on graphene oxide	CV and chronoamperometry	0.38	0.4–10	Serum samples	57
SnO_2 nanofibers-supported Au nanoparticles	Chronoamperometry	6.67	49.98–3937.21	Tap water, apple juice, *Lactobacillus plantarum*, *Bacillus subtilis*, and *Escherichia coli*	58
RGO/Au/Fe_3O_4/Ag nanocomposite	Amperometric Detection	1.43	2–12 000	Hair dye cream	59
MXene-Co_3O_4 nanocomposites	LSV	0.5	0–75	Cancer cell-lines	60
Micro & nano-CeO_2/GCE	CV and amperometry	0.4	0.001–0.125	NA	61
HRP/HAp5-fCNT/GC	Chronoamperometric detection	2	10–234	Raw-milk and pasteurized milk samples	62
CuCo-Cu@CoCH nanoarray	Amperometric	0.97	1–100	HepG2 human liver cancer cells	63
rGO-Co_3O_4-Pt nanocomposite	CV, EIS & SWV	0.16	0–2.5	DOX induced cardiac cell lines and mice heart tissue	This work

3.8 Batch-to-batch reproducibility, reusability and short-term storage study

The batch-to-batch consistency and reproducibility of the printed rGO-Co_3O_4-Pt electrodes were evaluated following procedures reported in recent electrochemical sensor studies.[64] Across four fabrication batches, the mean cathodic currents were −123.5, −107.8, −113.7, and −119.2 μA. The corresponding %RSD values were 1.1–3.3%, indicating excellent batch to batch reproducibility (Fig. S1).

Together, they show that our printing process yields consistent sensors, while longer term stability still needs to be evaluated. Reusability of the printed electrodes was assessed by recording successive responses to H_2O_2 on the same strip across three cycles (Fig. S2). At 0.2, 0.4, and 0.6 μM H_2O_2, the first-use cathodic currents were −2.13, −2.84, and −3.75 μA, respectively. Upon reuse, the responses decreased to −1.44, −1.72, and −2.31 μA in the second cycle, and further to −1.17, −1.39, and −1.66 μA in the third cycle. The attenuation is plausibly due to partial electrode fouling and/or minor detachment of the catalytic layer; despite this, the strips remain suitable for short-term repeated measurements.

Storage stability of the printed rGO-Co_3O_4-Pt strips was evaluated following the protocol of Xiong *et al.*[65] After 2 days, the electrodes retained approximately 91% of their initial response at 0.2 μM H_2O_2 and 87% at 0.4 μM, indicating robust short-term stability of the printed nanocomposite (Fig. S3). Together with their reproducibility and reusability, these data support the strips' suitability as practical, scalable platforms for ROS monitoring in biological settings.

3.9 *Ex vivo* real samples analysis

To assess the performance of the rGO-Co_3O_4-Pt/SPEs platform in a biological environment, SWV was used to evaluate oxidative stress in HL-1 cardiac cells under control conditions and following DOX challenge. DOX causes cardiotoxicity by generating excessive ROS, disrupting cellular homeostasis and damaging lipids, proteins, and DNA. It also triggers calcium dysregulation in cardiomyocytes, leading to oxidative stress and impaired cardiac function.[66,67] As illustrated in Fig. 6, the rGO-Co_3O_4-Pt-modified electrode exhibited significantly higher current responses in DOX-treated cells compared to either the bare electrode or untreated cells. These data clearly show that DOX increases ROS production, confirming the onset of oxidative stress and highlighting the sensitivity of the nanocomposites in effectively detecting H_2O_2. As expected, untreated control cells showed a low or negligible response. These results validate the selectivity of the rGO-Co_3O_4-Pt/SPEs platform, demonstrating its ability to minimize false-positive signals in the absence of elevated ROS. This selectivity is crucial for reliably distinguishing between normal and stressed cellular states.

3.10 *In vivo* and *ex vivo* studies

To assess the potential of the rGO-Co_3O_4-Pt/SPEs platform for *in vivo* applications, we evaluated its ability to monitor H_2O_2 levels in heart tissues of mice treated with DOX, used as model of cardiotoxicity. All animal experiments were carried out under Italian Ministry of Health authorization 36/2024-PR and in accordance with applicable regulations. Fig. 7A shows that the rGO-Co_3O_4-Pt-modified electrode detected significantly higher currents in samples obtained from DOX-treated mice compared to both control mice and the bare electrode, indicating elevated H_2O_2 levels due to increased oxidative stress. Heart tissue obtained from control mice showed minimal current responses, confirming low H_2O_2 levels and the selectivity of rGO-Co_3O_4-Pt/SPEs. The results demonstrate that the rGO-Co_3O_4-Pt/SPEs platform effectively detects elevated oxidative stress levels in heart tissue of DOX-treated mice, confirming its high sensitivity and selectivity for monitoring oxidative stress *in vivo*. This highlights its potential for applications in studying ROS-related pathologies and diagnostics.

The capability of the rGO-Co_3O_4-Pt/SPEs platform to monitor oxidative stress was supported by the evaluation of cell viability and ROS production in HL-1 cardiomyocytes treated or not with DOX (2 μM). DOX challenge significantly increased ROS production with no changes in cell viability of HL-1 cardiomyocytes, as shown in Fig. 7B. Light microscopy images (Fig. 7C) revealed morphological changes in DOX-treated cells, compared to control cells. Fluorescence

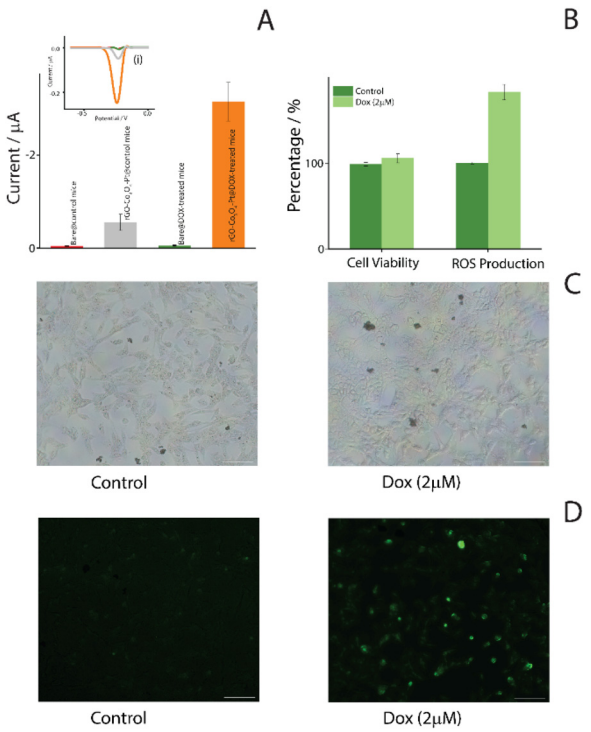

Fig. 7 (A) Potential of rGO-Co_3O_4-Pt/SPEs for *in vivo* monitoring of H_2O_2 in DOX-induced cardiotoxicity animal model. Inset (i) displays the corresponding SWV curves, with a sharp signal increase in the DOX-treated group; (B) *ex vivo* assessment of cell viability and ROS production in DOX-treated HL-1 cardiomyocytes; (C) light microscopy images of HL-1 cardiomyocytes: control *vs.* DOX treatment; (D) fluorescence microscopy for ROS detection in HL-1 cardiomyocytes.

microscopy (Fig. 7D) confirmed elevated ROS levels in DOX-insulted cells, with minimal fluorescence observed in controls. These results demonstrate the platform's ability to detect ROS variations and oxidative stress caused by DOX, that is crucial for understanding cardiotoxic effects.

The results show a strong correlation between the performance of the proposed rGO-Co_3O_4-Pt/SPEs biosensor and the traditional fluorescence-based method for detecting ROS in cells and tissues. This consistent alignment confirms the biosensor as a dependable and sensitive tool for monitoring cellular oxidative stress. Its ability to deliver results comparable to the traditional fluorescence assay underscores its potential for wider use in ROS research and diagnostics.

Although no murine model fully recapitulates human cardiotoxicity, our chosen regimen-DOX 5 mg kg^{-1} i.p. weekly for four weeks (20 mg kg^{-1} total), is among the best-documented and validated mouse protocols for anthracycline cardiotoxicity. It consistently elicits mitochondrial dysfunction, oxidative stress, and structural myocardial injury, supporting mechanistic studies of ROS-mediated damage.[68–70]

4 Conclusions

This study successfully highlighted the design, characterization and application of the novel nanocomposite rGO-Co_3O_4-Pt in combination with printed electrochemical strips for the detection of ROS in both *ex vivo* and *in vivo* models. ROS plays a significant role as a signalling molecules in physiological and pathological processes, whose variation is connected to and serves as an important marker for oxidative stress in the development and progression of atherosclerosis and other cardiovascular diseases. This nanoengineered sensing platform has been able to evaluate the real-time variation of ROS in both DOX-challenged cells and mice, demonstrating high selectivity and sensitivity in complex biological environments, minimizing false positives in the absence of elevated ROS amount. Satisfactory agreement with traditional fluorescence-based methods highlights the biosensor's accuracy and usefulness, successfully distinguishing between normal and stressed cells and tissues. This approach provides a robust foundation for advancing real-time ROS monitoring, thereby driving progress in cardiovascular research, oxidative stress diagnostics, and the development of novel therapeutic interventions for ROS-related diseases. This approach shows strong promise for wider disease management, including oncology. Portable, user-friendly analyzers built on nanomaterial-enabled sensors could support on-treatment monitoring of efficacy, dose titration, and patient-specific pharmacodynamic responses, thereby accelerating drug discovery and therapeutic development. The *in vivo* proof-of-concept is encouraging, but long-term biocompatibility and tissue retention/clearance must still be established. Our next phase will integrate wireless readout and extend continuous recordings beyond 24 hours.

Our printed rGO-Co_3O_4-Pt/SPE strips confirm the feasibility of real-time ROS monitoring, but clinical translation is premature. Key hurdles include ensuring biocompatibility, preventing Pt leaching, achieving durable *in vivo* stability, and meeting regulatory requirements for implantable sensors. Accordingly, this work remains a proof-of-concept; future studies must address these constraints before clinical application.

Author contributions

S. C.: funding acquisition, project administration, and supervision. S. S.: investigation, original draft preparation, and funding acquisition. S. M.: cell-line experimentation, *in vivo* studies, formal analysis, and manuscript review and editing. A. R.: formal analysis and critical review and editing of the manuscript. A. N.: materials synthesis, analytical assessments, and manuscript writing. M. K.: formal analysis and manuscript review and editing. B. H. G.: formal analysis and manuscript review and editing. R. M.: supervision and validation of *ex vivo* and *in vivo* experimental work. C. P.: supervision and validation of *ex vivo* and *in vivo* experimental work, formal analysis, and manuscript review and editing.

Conflicts of interest

There are no conflicts to declare.

Data availability

The data supporting the findings of this study are available within the article.

Supplementary information (SI): supplementary figures. See DOI: https://doi.org/10.1039/d5nr03297k.

Acknowledgements

S. C. acknowledges funding from AIRC under the MFAG 2022 (ID 27586) project. This project also received funding from the European Union's Horizon 2020 research and innovation program under the Marie Skłodowska-Curie grant agreement no. 101110684 (SMART – Sima Singh). S. C. acknowledges the "Pathogen Readiness Platform for CERIC-ERIC Upgrade" PRP@CERIC è finanziato dal PNRR Piano Nazionale di Ripresa e Resilienza nell'ambito della Missione 4 "Istruzione e Ricerca", Componente 2 "Dalla Ricerca all'Impresa", Linea di Investimento 3.1 "Fondo per la realizzazione di un sistema integrato di infrastrutture di ricerca e innovazione", finanziato dall'Unione Europea – Next Generation EU. MacDermid Alpha – Film & Smart Surface Solutions is acknowledged to have provided the polyester sheets Auto – stat HT5 as the substrate for screen-printing electrodes.

References

1 D. G. Deavall, E. A. Martin, J. M. Horner and R. Roberts, *J. Toxicol.*, 2012, **2012**, 645460.
2 C. Hao, X. Wu, M. Sun, H. Zhang, A. Yuan, L. Xu, C. Xu and H. Kuang, *J. Am. Chem. Soc.*, 2019, **141**, 19373–19378.
3 X. Li, J. Gao, C. Wu, C. Wang, R. Zhang, J. He, Z. J. Xia, N. Joshi, J. M. Karp and R. Kuai, *Sci. Adv.*, 2024, **10**, 1–17.
4 A. B. Jena, R. R. Samal, N. K. Bhol and A. K. Duttaroy, *Biomed. Pharmacother.*, 2023, **162**, 114606.
5 M. Sharifi-Rad, N. V. Anil Kumar, P. Zucca, E. M. Varoni, L. Dini, E. Panzarini, J. Rajkovic, P. V. Tsouh Fokou, E. Azzini, I. Peluso, A. Prakash Mishra, M. Nigam, Y. El Rayess, M. El Beyrouthy, L. Polito, M. Iriti, N. Martins, M. Martorell, A. O. Docea, W. N. Setzer, D. Calina, W. C. Cho and J. Sharifi-Rad, *Front. Physiol.*, 2020, **11**, 694.
6 F. J. Kelly and J. C. Fussell, *Free Radicals Biol. Med.*, 2017, **110**, 345–367.
7 R. D'Oria, R. Schipani, A. Leonardini, A. Natalicchio, S. Perrini, A. Cignarelli, L. Laviola and F. Giorgino, *Oxid. Med. Cell. Longevity*, 2020, **2020**, 5732956.
8 A. Chota, B. P. George and H. Abrahamse, in *Handbook of Oxidative Stress in Cancer: Therapeutic Aspects: Volume 1*, 2022, vol. 1, pp. 1–35.
9 H. Jiang, J. Zuo, B. Li, R. Chen, K. Luo, X. Xiang, S. Lu, C. Huang, L. Liu, J. Tang and F. Gao, *Redox Biol.*, 2023, **63**, 102754.
10 Y. Liu, A. Asnani, L. Zou, V. L. Bentley, M. Yu, Y. Wang, G. Dellaire, K. S. Sarkar, M. Dai, H. H. Chen, D. E. Sosnovik, J. T. Shin, D. A. Haber, J. N. Berman, W. Chao and R. T. Peterson, *Sci. Transl. Med.*, 2014, **6**, 266ra170.
11 C. Y. Kong, Z. Guo, P. Song, X. Zhang, Y. P. Yuan, T. Teng, L. Yan and Q. Z. Tang, *Int. J. Biol. Sci.*, 2022, **18**, 760–770.
12 M. Sheibani, Y. Azizi, M. Shayan, S. Nezamoleslami, F. Eslami, M. H. Farjoo and A. R. Dehpour, *Cardiovasc. Toxicol.*, 2022, **22**, 292–310.
13 L. F. Hu, H. R. Lan, X. M. Li and K. T. Jin, *Oxid. Med. Cell. Longevity*, 2021, **2021**, 2951697.
14 F. K. Alharbi, Z. S. Alshehri, F. F. Alshehri, S. Alhajlah, H. A. Khalifa, N. Dahran and W. A. M. Ghonimi, *Open Vet. J.*, 2023, **13**, 1718–1728.
15 A. M. Rahman, S. W. Yusuf and M. S. Ewer, *Int. J. Nanomed.*, 2007, **2**, 567–583.
16 S. Miyata, G. Takemura, K. I. Kosai, T. Takahashi, M. Esaki, L. Li, H. Kanamori, R. Maruyama, K. Goto, A. Tsujimoto, T. Takeyama, T. Kawaguchi, T. Ohno, K. Nishigaki, T. Fujiwara, H. Fujiwara and S. Minatoguchi, *Am. J. Pathol.*, 2010, **176**, 687–698.
17 M. Räsänen, J. Degerman, T. A. Nissinen, I. Miinalainen, R. Kerkelä, A. Siltanen, J. T. Backman, E. Mervaala, J. J. Hulmi, R. Kivelä and K. Alitalo, *Proc. Natl. Acad. Sci. U. S. A.*, 2016, **113**, 13144–13149.
18 Y. Wang, J. Liao, Y. Luo, M. Li, X. Su, B. Yu, J. Teng, H. Wang and X. Lv, *Int. J. Mol. Sci.*, 2023, **24**, 3257.
19 T. Wang, C. Yuan, J. Liu, L. Deng, W. Li, J. He, H. Liu, L. Qu, J. Wu and W. Zou, *Int. J. Mol. Sci.*, 2023, **24**, 897.
20 M. Martin, A. Villar, A. Sole-Calvo, R. Gonzalez, B. Massuti, J. Lizon, C. Camps, A. Carrato, A. Casado, M. T. Candel, J. Albanell, J. Aranda, B. Munarriz, J. Campbell and E. Diaz-Rubio, *Ann. Oncol.*, 2003, **14**, 833–842.
21 E. Ho, K. Karimi Galougahi, C. C. Liu, R. Bhindi and G. A. Figtree, *Redox Biol.*, 2013, **1**, 483–491.
22 M. Rojkind, J. A. Domínguez-Rosales, N. Nieto and P. Greenwel, *Cell. Mol. Life Sci.*, 2002, **59**, 1872–1891.
23 J. W. M. Yuen and I. F. F. Benzie, *Free Radical Res.*, 2003, **37**, 1209–1213.
24 Y. Yu, J. Peng, M. Pan, Y. Ming, Y. Li, L. Yuan, Q. Liu, R. Han, Y. Hao, Y. Yang, D. Hu, H. Li and Z. Qian, *Small Methods*, 2021, **5**, 2001212.
25 M. Wang, S. Qiu, H. Yang, Y. Huang, L. Dai, B. Zhang and J. Zou, *Chemosphere*, 2021, **270**, 129448.
26 O. Tantawi, A. Baalbaki, R. El Asmar and A. Ghauch, *Sci. Total Environ.*, 2019, **654**, 107–117.
27 X. Tian, Y. Qin, Y. Jiang, X. Guo, Y. Wen and H. Yang, *Food Chem.*, 2024, **438**, 137777.
28 X. Jiang, H. Wang, R. Yuan and Y. Chai, *Anal. Chem.*, 2018, **90**, 8462–8469.
29 O. G. Lyublinskaya, S. A. Antonov, S. G. Gorokhovtsev, N. A. Pugovkina, J. S. Kornienko, J. S. Ivanova, A. N. Shatrova, N. D. Aksenov, V. V. Zenin and N. N. Nikolsky, *Free Radicals Biol. Med.*, 2018, **128**, 40–49.
30 V. Vaishampayan, A. Kapoor and S. P. Gumfekar, *Can. J. Chem. Eng.*, 2023, **101**, 5208–5221.
31 W. Wang, Z. Ma, Q. Shao, J. Wang, L. Wu, X. Huang, Z. Hu, N. Jiang, J. Dai and L. He, *Nanoscale*, 2024, **16**, 12586–12598.
32 N. Noor, E. Pajootan, P. Mirzaei and S. H. Bahrami, *Can. J. Chem. Eng.*, 2023, **101**, 5759–57719.
33 Z. Wang, L. Yan, Y. Liu, J. Wang, D. Li, Y. Wang, X. Wang, L. Li, S. Regmi, J. Ju and T. Zhan, *ACS Sustainable Chem. Eng.*, 2023, **11**, 15556–15565.
34 P. Li, L. Chen, Q. Yao, H. U. Khan, D. Chen and Y. Guo, *J. Electroanal. Chem.*, 2024, **958**, 118153.
35 Y. Lei, D. Butler, M. C. Lucking, F. Zhang, T. Xia, K. Fujisawa, T. Granzier-Nakajima, R. Cruz-Silva, M. Endo, H. Terrones, M. Terrones and A. Ebrahimi, *Sci. Adv.*, 2020, **6**, eabc4250.
36 H. Maseed, V. M. Reddy Yenugu, S. S. B. Devarakonda, S. Petnikota, M. Gajulapalli and V. V. S. S. Srikanth, *ACS Appl. Nano Mater.*, 2023, **6**, 18531–18538.
37 Y. Liang, Y. Li, H. Wang, J. Zhou, J. Wang, T. Regier and H. Dai, *Nat. Mater.*, 2011, **10**, 780–786.
38 M. Mehmood Shahid, A. H. Ismail, A. M. A. A. Al-Mokaram, R. Vikneswaran, S. Ahmad, A. Hamza and A. Numan, *Prog. Nat. Sci.:Mater. Int.*, 2017, **27**, 582–587.
39 P. Mohana, S. Swathi, R. Yuvakkumar, G. Ravi, M. Thambidurai and H. D. Nguyen, *Int. J. Hydrogen Energy*, 2024, **49**, 376–389.
40 A. Valipour, N. Hamnabard and Y. H. Ahn, *RSC Adv.*, 2015, **5**, 92970–92979.
41 S. Xie, S. Il Choi, X. Xia and Y. Xia, *Curr. Opin. Chem. Eng.*, 2013, **2**, 142–150.

42 M. Fahad, M. Tassaduq, A. Basit, M. Ibrahim and F. Muhammad, *J. Mater. Sci. Res. Rev.*, 2024, **7**, 227–237.
43 H. Zhou, H. Zheng, W. Shi and X. Ma, *Scr. Mater.*, 2025, **255**, 116397.
44 B. J. Schultz, R. V. Dennis, J. P. Aldinger, C. Jaye, X. Wang, D. A. Fischer, A. N. Cartwright and S. Banerjee, *RSC Adv.*, 2014, **4**, 1286–1292.
45 Y. Z. Liu, C. M. Chen, Y. F. Li, X. M. Li, Q. Q. Kong and M. Z. Wang, *J. Mater. Chem. A*, 2014, **2**, 5739–5746.
46 H. Singh, A. K. Sinha, S. M. Gupta, M. N. Singh and H. Ghosh, *Condens. Matter Sci.*, 2015, **6**, 1–8.
47 R. J. Isaifan, S. Ntais and E. A. Baranova, *Appl. Catal., A*, 2013, **464–465**, 68–74.
48 A. I. Boronin, E. M. Slavinskaya, A. Figueroba, A. I. Stadnichenko, T. Y. Kardash, O. A. Stonkus, E. A. Fedorova, V. V. Muravev, V. A. Svetlichnyi, A. Bruix and K. M. Neyman, *Appl. Catal., B*, 2021, **286**, 119931.
49 S. Mahalingam, S. Ayyaru and Y. H. Ahn, *Sustainable Energy Fuels*, 2020, **4**, 1532–1542.
50 H. Lee, K. H. Kim, W. H. Choi, B. C. Moon, H. J. Kong and J. K. Kang, *ACS Appl. Mater. Interfaces*, 2019, **11**, 43998–44008.
51 X. Chang, C. Batchelor-McAuley and R. G. Compton, *Chem. Sci.*, 2020, **11**, 4416–4421.
52 J. Mu, Y. Wang, M. Zhao and L. Zhang, *Chem. Commun.*, 2012, **48**, 2540–2542.
53 Q. Wang, J. Chen, H. Zhang, W. Wu, Z. Zhang and S. Dong, *Nanoscale*, 2018, **10**, 19140–19146.
54 N. Alyamni, J. L. Abot and A. G. Zestos, *ECS Sens. Plus*, 2024, **3**, 27001.
55 H. Gao, H. Yu, S. Yang, F. Chai, H. Wu and M. Tian, *Microchim. Acta*, 2024, **191**, 6541.
56 N. Sobahi, M. Imran, M. E. Khan, A. Mohammad, M. M. Alam, T. Yoon, I. M. Mehedi, M. A. Hussain, M. J. Abdulaal and A. A. Jiman, *Materials*, 2023, **16**, 2770.
57 Y. Zhang, Y. Duan, Z. Shao, C. Chen, M. Yang, G. Lu, W. Xu and X. Liao, *Microchim. Acta*, 2019, **186**, 3502.
58 M. A. Kader, N. S. Azmi, A. K. M. Kafi, M. S. Hossain, M. F. Bin Masri, A. N. M. Ramli and C. S. Tan, *Chemosensors*, 2023, **11**, 130.
59 K. Heydaryan, M. Almasi Kashi, N. Sharifi and M. Ranjbar-Azad, *New J. Chem*, 2020, **44**, 9471–9480.
60 S. Singh, A. Numan, M. Khalid, I. Bello, E. Panza and S. Cinti, *Small*, 2023, **19**, 2208209.
61 S. Rajendran, D. Manoj, R. Suresh, Y. Vasseghian, A. A. Ghfar, G. Sharma and M. Soto-Moscoso, *Environ. Res.*, 2022, **214**, 113961.
62 J. Alvarez-Paguay, L. Fernández, D. Bolaños-Méndez, G. González and P. J. Espinoza-Montero, *Sens. Biosensing Res.*, 2022, **37**, 100514.
63 N. Han, S. Hu, L. Zhang, S. Yi, Z. Zhang, Y. Wang, Y. Zhou, D. Chen and Y. Gao, *Appl. Surf. Sci.*, 2022, **576**, 151879.
64 M. Tuccillo, P. M. Kalligosfyri, A. Miglione, C. Di Natale, M. Spinelli, A. Amoresano, D. Calabria, M. Mirasoli, I. A. Darwish and S. Cinti, *Electrochim. Acta*, 2025, **541**, 147285.
65 L. Xiong, Y. Zhang, S. Wu, F. Chen, L. Lei, L. Yu and C. Li, *Int. J. Mol. Sci.*, 2022, **23**, 3799.
66 T. Šimůnek, M. Štěrba, O. Popelová, M. Adamcová, R. Hrdina and V. Gerši, *Pharmacol. Rep.*, 2009, **61**, 154–171.
67 P. Angsutararux, S. Luanpitpong and S. Issaragrisil, *Oxid. Med. Cell. Longevity*, 2015, **2015**, 795602.
68 Y. Octavia, C. G. Tocchetti, K. L. Gabrielson, S. Janssens, H. J. Crijns and A. L. Moens, *J. Mol. Cell Cardiol.*, 2012, **52**, 1213–1225.
69 S. Zhang, X. Liu, T. Bawa-Khalfe, L. S. Lu, Y. L. Lyu, L. F. Liu and E. T. H. Yeh, *Nat. Med.*, 2012, **18**, 1639–1642.
70 P. Vejpongsa and E. T. H. Yeh, *J. Am. Coll. Cardiol.*, 2014, **64**, 938–945.